Article

Cell Reports

Structural Insights into Divalent Cation Modulations of ATP-Gated P2X Receptor Channels

Graphical Abstract

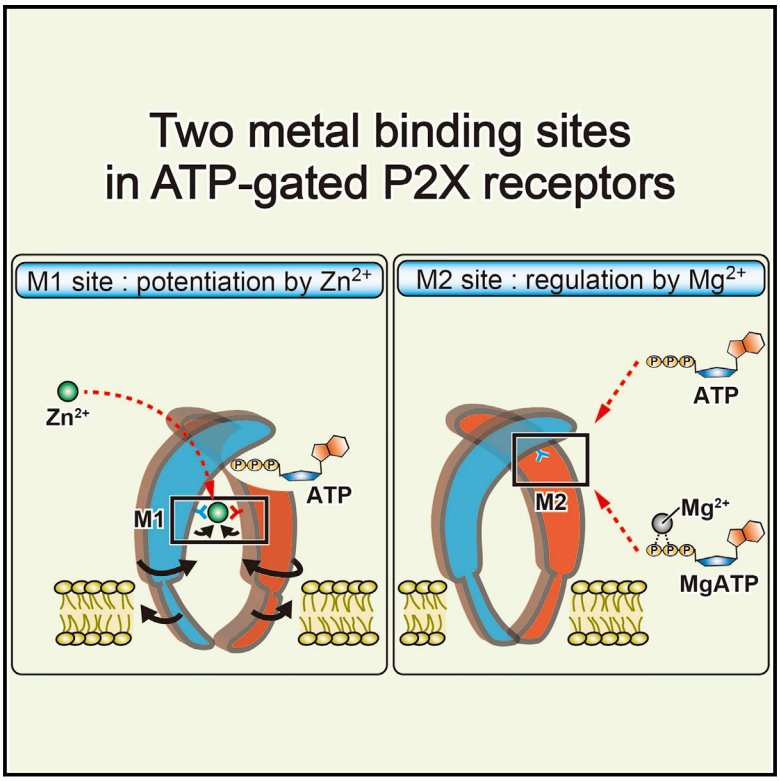

Authors

Go Kasuya, Yuichiro Fujiwara, Mizuki Takemoto, ..., Ryuichiro Ishitani, Motoyuki Hattori, Osamu Nureki

Correspondence

hattorim@fudan.edu.cn (M.H.), nureki@bs.s.u-tokyo.ac.jp (O.N.)

In Brief

Kasuya et al. report the structure of an invertebrate P2X receptor in the presence of ATP and Zn^{2+} ion, revealing two distinct metal binding sites. The first site, located at the trimer interface, is responsible for Zn^{2+} potentiation, whereas the second site is coupled with ATP binding for regulation by Mg^{2+}.

Highlights

- The ATP- and Zn^{2+}-bound structure of an invertebrate P2X receptor is determined
- Two distinct metal binding sites in the extracellular region are identified
- The first site, located at the trimer interface, contributes to Zn^{2+} potentiation
- The second site is coupled with ATP binding for regulation by Mg^{2+}

Accession Numbers

5F1C

Kasuya et al., 2016, Cell Reports *14*, 932–944
February 2, 2016
http://dx.doi.org/10.1016/j.celrep.2015.12.087

OPEN ACCESS
CellPress

Cell Reports
Article

Structural Insights into Divalent Cation Modulations of ATP-Gated P2X Receptor Channels

Go Kasuya,[1,7] Yuichiro Fujiwara,[2,7] Mizuki Takemoto,[1] Naoshi Dohmae,[3] Yoshiko Nakada-Nakura,[4] Ryuichiro Ishitani,[1] Motoyuki Hattori,[5,6,*] and Osamu Nureki[1,*]

[1]Department of Biological Sciences, Graduate School of Science, The University of Tokyo, 2-11-16 Yayoi, Bunkyo-ku, Tokyo 113-0032, Japan
[2]Department of Physiology, Graduate School of Medicine, Osaka University, 2-2 Yamadaoka, Suita, Osaka 565-0871, Japan
[3]Global Research Cluster, RIKEN, 2-1 Hirosawa, Wako-shi, Saitama 351-0198, Japan
[4]Department of Cell Biology, Graduate School of Medicine, Kyoto University, Konoe-cho, Yoshida Sakyo-ku, Kyoto 606-8501, Japan
[5]State Key Laboratory of Genetic Engineering, Collaborative Innovation Center for Genetics and Development, Department of Physiology and Biophysics, School of Life Sciences, Fudan University, 2005 Songhu Road, Yangpu District, Shanghai 200438, China
[6]Precursory Research for Embryonic Science and Technology, Japan Science and Technology Agency, 4-1-8 Honcho, Kawaguchi, Saitama 332-0012, Japan
[7]Co-first author
*Correspondence: hattorim@fudan.edu.cn (M.H.), nureki@bs.s.u-tokyo.ac.jp (O.N.)
http://dx.doi.org/10.1016/j.celrep.2015.12.087

SUMMARY

P2X receptors are trimeric ATP-gated cation channels involved in physiological processes ranging widely from neurotransmission to pain and taste signal transduction. The modulation of the channel gating, including that by divalent cations, contributes to these diverse physiological functions of P2X receptors. Here, we report the crystal structure of an invertebrate P2X receptor from the Gulf Coast tick *Amblyomma maculatum* in the presence of ATP and Zn^{2+} ion, together with electrophysiological and computational analyses. The structure revealed two distinct metal binding sites, M1 and M2, in the extracellular region. The M1 site, located at the trimer interface, is responsible for Zn^{2+} potentiation by facilitating the structural change of the extracellular domain for pore opening. In contrast, the M2 site, coupled with the ATP binding site, might contribute to regulation by Mg^{2+}. Overall, our work provides structural insights into the divalent cation modulations of P2X receptors.

INTRODUCTION

P2X receptors are trimeric cation channels that respond to extracellular ATP and play a crucial role in initiating extracellular ATP signaling (Brake et al., 1994; Chen et al., 1995; Valera et al., 1994). In vertebrates, the seven subtypes of P2X receptors form homo- or hetero-trimers, with each protomer consisting of two transmembrane helices and a large, hydrophilic extracellular domain (North, 2002). The transmembrane domain is responsible for the formation of a non-selective cation pore, whereas the extracellular domain includes binding sites for ATP, regulatory metal ions, and antagonists (Egan et al., 2006). P2X receptors exhibit various biophysical and pharmacological properties and are widely expressed in the human body. Accordingly, P2X receptors are involved in diverse physiological processes, such as muscle contraction, neurotransmission, inflammatory response, and pain and taste signal transduction (Khakh and North, 2012; Surprenant and North, 2009). Therefore, they are associated with numerous human diseases, including chronic inflammatory and neuropathic pain, depression, and cancer (Burnstock, 2006; Burnstock and Ralevic, 2014; Gever et al., 2006; North and Jarvis, 2013).

The activation of ligand-gated ion channels, including P2X receptors, Cys-loop receptors, and ionotropic glutamate receptors, is modulated by various molecules to diversify their physiological functions (Jarvis and Khakh, 2009; Miller and Smart, 2010; Traynelis et al., 2010). In particular, divalent cations are important regulatory factors in these ion channel superfamilies. For instance, in some P2X receptors, such as the P2X2 and P2X4 receptors, a Zn^{2+} ion potentiates the ATP-dependent currents (Garcia-Guzman et al., 1997; Nakazawa and Ohno, 1997; Séguéla et al., 1996; Soto et al., 1996). The Zn^{2+} modulation of P2X4 receptors may play a role in the enhancement of long-term potentiation (Lorca et al., 2011) and insulin secretion (Richards-Williams et al., 2008).

The recently determined structures of the zebrafish P2X4 (zfP2X4) receptor in the apo, closed state and the ATP-bound, open state provided the structural framework for trimer formation, ATP recognition, and ATP-dependent activation in the P2X receptor family (Hattori and Gouaux, 2012; Jiang et al., 2013; Kawate et al., 2009; Samways et al., 2014). The subsequent structure-based electrophysiological and computational analyses provided further clarification of the activation mechanism of P2X receptors (Heymann et al., 2013; Lörinczi et al., 2012; Roberts et al., 2012; Zhao et al., 2014). However, the molecular mechanisms of the divalent cation modulation of the P2X receptors, underlying the diversity of the receptor functions, have still proved elusive.

P2X receptors have also been cloned from invertebrate species (Agboh et al., 2004; Bavan et al., 2009; Bavan et al., 2012; Fountain

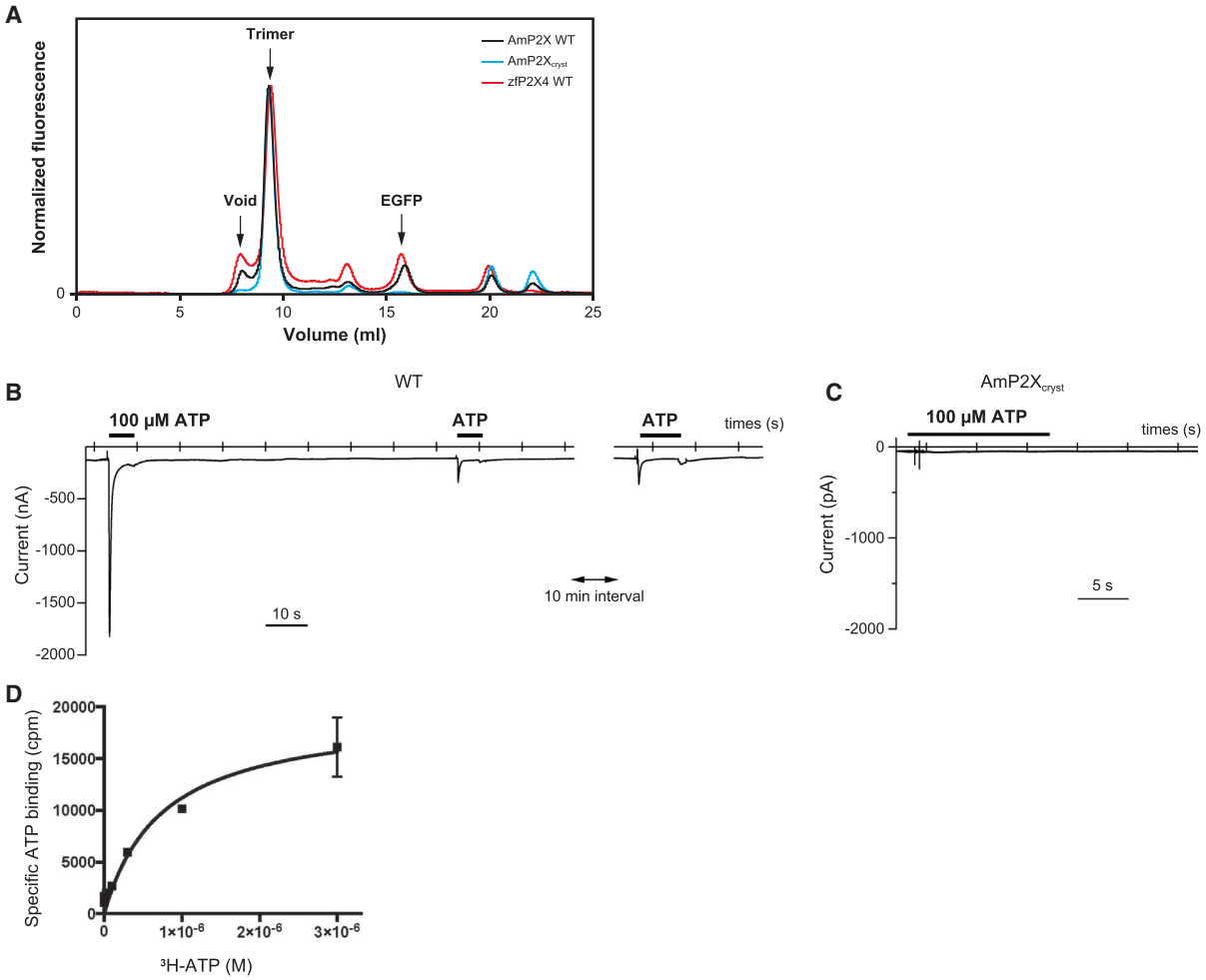

Figure 1. Functional Properties of AmP2X and Crystallization Construct AmP2X$_{cryst}$

(A) FSEC profiles on a Superdex 200 10/300 GL column (GE Healthcare) for the EGFP-fused AmP2X WT (black), the EGFP-fused AmP2X$_{cryst}$ (blue), and the EGFP-fused zfP2X4 WT (red), expressed in HEK293T cells. The arrows indicate the estimated elution positions of the void volume, the EGFP-fused P2X (trimer), and the free EGFP.

(B) Representative currents of the AmP2X WT evoked by 100 μM ATP.

(C) Representative current traces of AmP2X$_{cryst}$ with the application of 100 μM ATP, showing no evoked current.

(D) Measurement of the ATP binding ability of the EGFP-fused AmP2X$_{cryst}$ by a ^{3}H-ATP binding assay. Error bars indicate ±SEM for triplicate samples. The calculated K_d for ^{3}H-ATP binding is 0.745 ± 0.238 μM.

et al., 2007; Raouf et al., 2005). They share low sequence identity with their vertebrate counterparts and seem to represent orthologs to ancestral P2X receptors. Like their vertebrate counterparts, the invertebrate P2X receptors function as ATP-gated, non-selective cation channels, and their biophysical properties include divalent cation modulations. Accordingly, the invertebrate P2X receptors can be a useful model for structural and electrophysiological studies to clarify the molecular mechanisms of the divalent cation modulations of the vertebrate P2X receptors.

Here we report the crystal structure of the P2X receptor from the Gulf Coast tick, *Amblyomma maculatum* (AmP2X), an invertebrate harboring one copy of the P2X receptor gene. Together with electrophysiological and computational analyses, our study provides structural insights into the divalent cation modulations of P2X receptors.

RESULTS

Functional Characterization and Structure Determination of AmP2X

Fluorescence-detection size-exclusion chromatography (FSEC) of an N-terminally GFP-tagged P2X receptor from AmP2X showed a sharp, symmetrical profile (Kawate and Gouaux, 2006), comparable to that of the zfP2X4 receptor with its known crystal structures (Hattori and Gouaux, 2012; Kawate et al., 2009), indicating that AmP2X is a promising target for structural analysis (Figure 1A). The two-electrode voltage clamp (TEVC) recording of *Xenopus* oocytes expressing AmP2X revealed that AmP2X functions as an ATP-gated cation channel with fast inactivation, or in other words, desensitization (Figure 1B), while the amino acid sequence of AmP2X is most closely related

to that of the slowly desensitizing P2X4 receptor among the mammalian P2X receptors (~40% sequence identity) (Figures S1 and S2). In addition, a huge current decline occurred in the AmP2X-current amplitude, in response to the second and subsequent ATP applications, even after a 10 min interval (Figure 1B). This shows the strong channel rundown in the AmP2X receptor. Channel rundown has been reported for other P2X receptors, such as P2X1, P2X3, P2X5, and some mutant P2X receptors, as well as for other ligand-gated ion channels (Bo et al., 2000; Fujiwara and Kubo, 2006; Jensik and Cox, 2002; Lewis and Evans, 2000; Mo et al., 2009). It is typically caused by slow recovery from inactivation or channel internalization, as observed in other P2X receptors (Bernier et al., 2008; Fujiwara and Kubo, 2006; Jensik and Cox, 2002; Mo et al., 2009).

To further investigate this channel property of AmP2X, we conducted simultaneous fluorescent imaging and electrical recordings of *Xenopus* oocytes expressing GFP-tagged AmP2X receptors (Figure S3). The results showed that wild-type (WT) AmP2X was expressed at the cell surface and repetitive ATP applications did not induce the internalization of AmP2X (Figure S3A), indicating that fast inactivation and slow recovery from inactivation caused the strong channel rundown of AmP2X.

The removal of 23 N-terminal and 7 C-terminal residues and the mutations of Asn171 and Cys374 ($AmP2X_{cryst}$, ΔN23/ΔC7/N171Q/C374L) yielded crystals diffracting up to 2.8 Å resolution in the presence of ATP and Zn^{2+} ion (Table S1). The deletion of 23 N-terminal and 7 C-terminal residues was designed basically according to the zfP2X4-C crystallization construct of zfP2X4 (Hattori and Gouaux, 2012). C374L was designed to remove the free cysteine residue to avoid non-specific disulfide formation. Asn171, a putative glycosylation site, was mutated to reduce the heterogeneity of the construct for crystallization. Although $AmP2X_{cryst}$ still exhibited ATP binding activity and cell surface expression (Figures 1D and S3B), it did not show ATP-dependent gating activity (Figure 1C). The structure of $AmP2X_{cryst}$ was solved by molecular replacement, using the ATP-bound zfP2X4 structure as the search model (Figures S4A–S4C).

Overall Structure and ATP Binding Site

$AmP2X_{cryst}$ adopts a chalice-like trimeric architecture, and each subunit of $AmP2X_{cryst}$ consists of a large extracellular domain and two transmembrane helices resembling the shape of a dolphin, as observed in the zfP2X4 structure (Figures 2A, 2B, and S4D) (Hattori and Gouaux, 2012; Kawate et al., 2009). We observed strong electron density peaks corresponding to ATP molecules at each subunit interface of the extracellular domain (Figure 2C), consistent with the crystallization conditions containing 1 mM ATP and the ATP binding activity of the $AmP2X_{cryst}$ construct (Figure 1D). The ATP molecules adopt a bent conformation and form tight interactions with the receptor (Figure 2C). The phosphate groups are recognized by the side chains of Lys66, Lys68, and Lys210 from one subunit and Asn311, Arg313, and Lys327 from the neighboring subunit, whereas the adenine ring of ATP forms hydrogen bonds with the side chain of Thr206 and the main chain carbonyl atoms of Lys66 and Thr206 (Figure 2C). All of these hydrophilic residues are highly conserved among P2X receptors (Figure S1) and are important for their ATP-dependent gating activities (Ennion et al., 2000; Jiang et al., 2000; Marquez-Klaka et al., 2007; Roberts et al., 2008; Roberts and Evans, 2004, 2006, 2007).

While the extracellular domain structure of $AmP2X_{cryst}$ resembles that of the ATP-bound, open zfP2X4, rather than that of apo, closed zfP2X4 (Figure S4E), the transmembrane domain of $AmP2X_{cryst}$ exhibits a unique feature. The root-mean-square deviations (RMSDs) for the 138 Cα atoms from the transmembrane domain of the trimer are 2.2 Å between AmP2X and ATP-bound zfP2X4 and 4.9 Å between AmP2X and apo, closed zfP2X4 (Figures 2E, 2F, and 3A–3C). Thus, the structure of the transmembrane domain of the AmP2X trimer is closer to that of ATP-bound, open zfP2X4 (Figures 2E, 2F, and 3A–3C). In contrast, the transmembrane domain of each AmP2X monomer resembles that of the apo, closed state of zfP2X4 (Figures 2D and 3J–3L). The RMSDs for the 46 Cα atoms from the transmembrane domain of each monomer are 2.1 Å between AmP2X and ATP-bound zfP2X4 and 1.7 Å between AmP2X and apo, closed zfP2X4.

The superimposition of the transmembrane architecture of $AmP2X_{cryst}$ with those of the previously determined zfP2X4 structures revealed further details about their structural differences. Consistent with the ATP-dependent expansion of the extracellular domain, the TM1 and TM2 helices in the $AmP2X_{cryst}$ structure are rotated by ~5 and ~40 degrees counterclockwise around the pore-center axis, relative to the closed state, whereas those in the ATP-bound zfP2X4 are rotated by ~10 and ~55 degrees counterclockwise around the pore-center axis, respectively (Figure 2F). These movements induce an iris-like expansion of the transmembrane helices by ~3 Å to form a pore (Figures 3A–3C). Consistent with the smaller rotation angles, the pore size at the constriction region is smaller in the $AmP2X_{cryst}$ structure (Figures 3D–3I). The TM2 helices are totally straight in the $AmP2X_{cryst}$ structure, which restricts the wide pore formation (Figures 3B, 3E, 3H, 3K, and 3N), while the kink of TM2 at the highly conserved Gly350 residue in zfP2X4 enables the TM2 helices to form the larger pore (Figures 3C, 3F, 3I, 3L, and 3O). In AmP2X, the residue corresponding to Gly350 in zfP2X4 is replaced by Val (Figure S1). Overall, the ion-conducing pore is partially opened in the $AmP2X_{cryst}$ structure with the straight TM2 helices.

Because the ion-conducting pore is partially opened, the present structure of $AmP2X_{cryst}$ might reflect either a pre-open state before channel opening or an inactivated state after channel opening. Considering the loss of the channel gating activity and the structural features, including the activated extracellular domain (Figures 1D and S4E), we regard the pre-open state, in which an ATP-induced conformational change in the extracellular cellular domain is partially propagated to the transmembrane domain, to be more likely.

Furthermore, it was proposed that the transmembrane architecture of the previously determined ATP-bound structure of the zfP2X4 trimer, including the large inter-subunit gaps, is partially distorted from that in the membrane-embedded native state (Heymann et al., 2013). Because the trimeric architecture of $AmP2X_{cryst}$ resembles that of the ATP-bound structure of zfP2X4 (Figures 3E and 3F), similar inter-subunit gaps are observed in the transmembrane region of the trimeric $AmP2X_{cryst}$ structure (Figure 3E). Accordingly, we do not exclude the

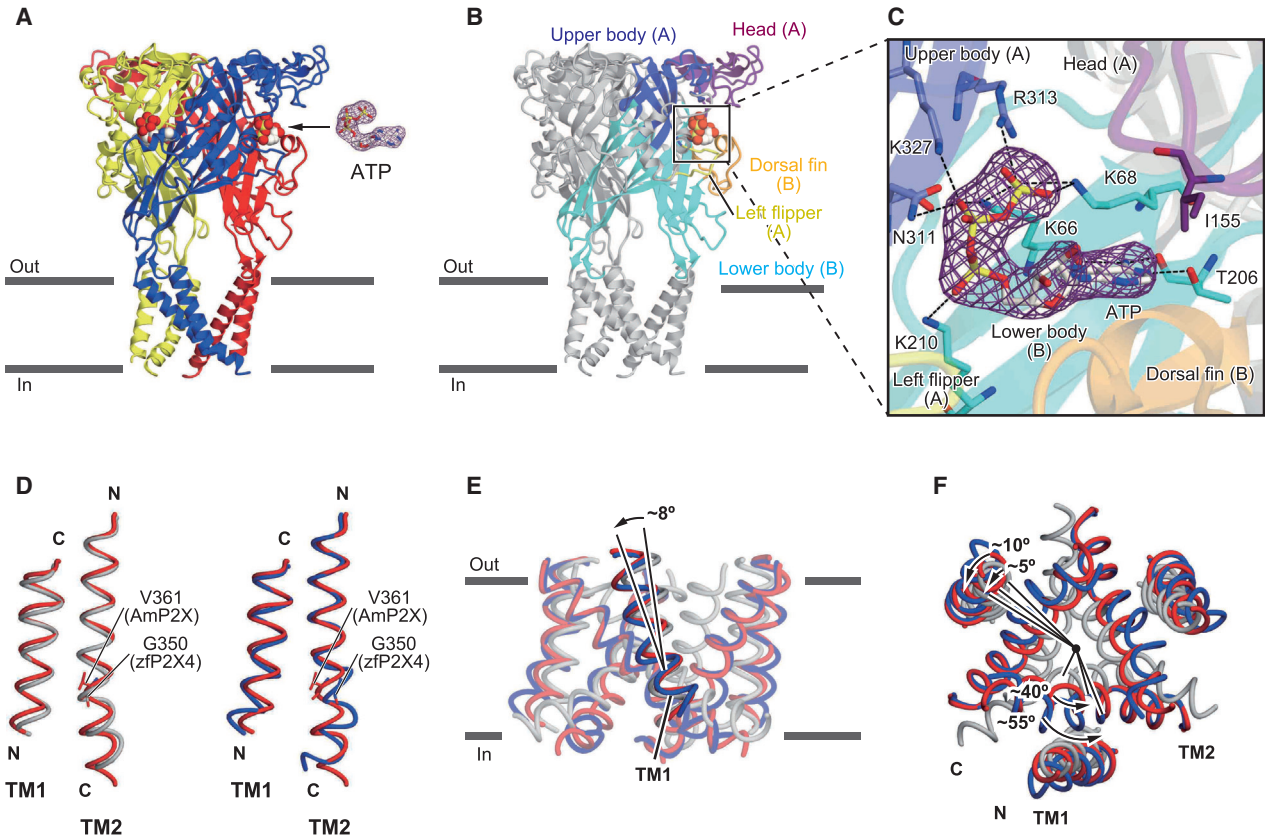

Figure 2. Overall Structure and ATP Binding Sites

(A) The ATP-bound AmP2X$_{cryst}$ structure viewed parallel to the membrane. The omit $F_o - F_c$ map contoured at 4σ, showing the electron density of the ATP.

(B and C) Close-up view of the ATP binding site in the ATP-bound AmP2X$_{cryst}$. The amino acid residues and ATP are depicted by stick models. The molecule is colored according to the dolphin-like model. Dotted black lines (C) indicate hydrogen bonds (<3.3 Å).

(D) Structural transition in the transmembrane helices. The transmembrane helices of the ATP-bound AmP2X$_{cryst}$ (red) are superimposed on those of apo, closed ΔP2X$_4$-B$_2$ (gray) and of ATP-bound ΔP2X$_4$-C (blue) using the Cα positions of residues 32–51 and 345–370 for AmP2X and residues 36–55 and 334–359 for zfP2X4, respectively. Gly350 in the two zfP2X4 structures and Val361 in the AmP2X structure are depicted by stick models.

(E and F) Structural comparison of the transmembrane domains as trimers viewed parallel to the membrane (E) and from the intracellular side (F). The transmembrane domain of the ATP-bound AmP2X$_{cryst}$ (red) is superimposed as a trimer on those of apo, closed ΔP2X$_4$-B$_2$ (gray) and of ATP-bound ΔP2X$_4$-C (blue) using the Cα positions of residues 32–51 and 345–370 for AmP2X and residues 36–55 and 334–359 for zfP2X4, respectively. The black arrows and bars denote the rotation of the transmembrane helices.

possibility that the trimer formation of the transmembrane domain in the AmP2X$_{cryst}$ structure is also partially distorted, possibly because of detergents or truncations employed for crystallization.

Zn^{2+} Binding Site and Modulation

In the ATP-bound AmP2X$_{cryst}$ structure crystallized in the presence of Zn^{2+} ion, we observed strong residual electron densities at two distant sites in the extracellular domain (Figure 4A). The anomalous difference Fourier map clearly showed that these densities correspond to Zn^{2+} ions (Figures 4B–4D). Accordingly, we identified two distinct metal binding sites in the extracellular domain of AmP2X$_{cryst}$ and named them the M1 and M2 sites. The M1 site is located at the trimer interface at the top part of the upper body domain of the dolphin model, in other words, the central chamber region (Figure 4A), and is coordinated by the side chains of Glu105 in one subunit and Glu106 in the neighboring subunit (Figures 4C and 4D). Among the P2X4 receptors, the corresponding residues at the M1 site are strictly conserved as Gln and Glu residues, respectively (Figure S1). The M2 site is coupled with the ATP binding site, and is surrounded by the side chain of Asp188 and the γ-phosphate group of ATP, to bridge the receptor and ATP molecules (Figure 4B). Asp188 is strictly conserved among the P2X1 and P2X3 receptors (Figure S1).

To investigate the functional roles of these metal binding sites, we first conducted structure-based electrophysiological analyses of Zn^{2+} potentiation. Because a huge current decline occurred in the AmP2X-current amplitudes, in response to the second and subsequent ATP applications (Figure 1B), AmP2X would not be suitable to analyze the Zn^{2+} potentiation by repetitive ATP applications. Therefore, we employed rat P2X4, which has well-established electrophysiological properties, including Zn^{2+} potentiation (Garcia-Guzman et al., 1997; Soto et al., 1996). We created the mutants (^{r}E95A, ^{r}D170A, and

^{r}E95A/^{r}D170A) of ^{r}Glu95 and ^{r}Asp170 for the equivalent residues in rat P2X4, corresponding to Glu106 in the M1 site and Asp188 in the M2 site of AmP2X, respectively (the superscript "r" refers to rat P2X4). The mutation at the M1 site (^{r}E95A) abolished the potentiation effect of Zn^{2+} ion (Figures 5A and 5B), whereas the mutation at the M2 site (^{r}D170A) did not affect the Zn^{2+} potentiation of the ATP-dependent currents (Figures 5A and 5B).

Glu105 and Glu106 at the M1 site in AmP2X are conserved as similar residues, Gln and Glu, respectively, among P2X4 receptors and some invertebrate P2X receptors (Figure S1). The Gln and Glu pair in the M1 site of these receptors would also provide chemically favorable conditions for Zn^{2+} binding, as observed in the AmP2X structure (Figures 4C and 4D). Consistently, our electrophysiological analysis revealed that the M1 site is responsible for the Zn^{2+} potentiation of the rat P2X4 receptor (Figures 5A and 5B). Furthermore, an invertebrate P2X receptor, LsP2X from the great pond snail, *Lymnaea stagnalis*, which possesses the M1 site (Figure S1), is also reportedly potentiated by Zn^{2+} ion (Bavan et al., 2012). Overall, our results suggest the functional role of the M1 site in zinc potentiation for the P2X4 receptors and the invertebrate P2X receptors possessing the M1 site.

The M1 site is overlapped with or neighboring the previously identified metal binding sites for Gd^{3+} and Mg^{2+} in the central chamber region, which are implicated in the inhibition of P2X receptors (Figures 4E–4G) (Kawate et al., 2009; Li et al., 2013). The M1 site shares some residues (^{r}Glu95 in rat P2X4) with the Gd^{3+} binding site (^{zf}Glu98 in zfP2X4) identified in the previously determined zfP2X4 structure in the apo, closed state (Figures 4E–4G) (Kawate et al., 2009). The application of Gd^{3+} inhibited the ATP-dependent activation of zfP2X4. Accordingly, the Gd^{3+} binding site seemed to play an important role in Gd^{3+} modulation (Kawate et al., 2009). However, we found that the mutation of ^{r}Glu95 did not abolish the Gd^{3+}-dependent inhibition (Figures S5A–S5D). The addition of 1 mM Gd^{3+} ion to a 100 μM ATP solution totally depleted the ATP because of precipitation (Figure S5E). Furthermore, the values of the Hill coefficients were out of order (about <35), suggesting that $GdCl_3$ does not affect the specific binding reaction between the ATP and the P2X receptor. Therefore, the depletion of ATP by Gd^{3+} addition, rather than the Gd^{3+} binding to the receptors, could be mainly responsible for the inhibitory effect of Gd^{3+} on the ATP-dependent activation of P2X receptors. More importantly, the Thr87 residue in the human P2X3 receptor, corresponding to Ser107 in AmP2X and Asp99 in zfP2X4 (Figures 4F and 4G), is implicated in the Mg^{2+}-dependent inhibition (Li et al., 2013). The Thr87 residue is located within the central chamber region and neighbors the M1 site and the Gd^{3+} binding site (Figures 4A and 4C–4G). Accordingly, the central chamber region in the extracellular domain may provide multiple cation binding sites for both potentiation and inhibition in P2X receptors.

Zn^{2+} Modulation Mechanism

To investigate how Zn^{2+} ion at the M1 site modulates channel gating, we performed all-atom molecular dynamics (MD) simulations of the ATP-bound $AmP2X_{cryst}$ in the presence and absence of Zn^{2+} at the M1 site (Figure 6). To analyze the initial early events upon zinc binding in the zinc potentiation of P2X receptors, the MD simulations were performed for 150 ns. We calculated the radial distance r of the center axis, and the polar angle θ and the azimuthal angle ϕ of the helical axis, to quantitatively estimate the structural change in the transmembrane region (Figures S4F and S4G) (Dai and Zhou, 2014). The results of the MD simulations revealed higher radial distance r and greater polar angle θ in the presence of Zn^{2+} ion (Figures 6A–6C), indicating that Zn^{2+} binding at the M1 site promotes channel opening (Figures 6D–6F). A further structural comparison of the extracellular domain revealed how Zn^{2+} binding to the extracellular domain facilitates channel opening in the transmembrane domain. First, Zn^{2+} binding to the M1 site brings two glutamate residues, Glu105 from one subunit and Glu106 from the neighboring subunit, toward each other by electrostatic attraction (Figures 6G, 6H, and 6M). This attraction induces the small counterclockwise rotation of the lower body domain by ~2 degrees (Figure 6I), whereas the side chains of the residues are turned away from each other in the absence of Zn^{2} (Figures 6G, 6H, and 6K). The Zn^{2+}-dependent small structural change within the upper lower body is magnified into the larger movement in the lower part of the body domain, which is directly connected to the transmembrane domain. Accordingly, the transmembrane domain is rotated counterclockwise by ~10 degrees to open the pore (Figures 6J and 6M).

Zn^{2+} potentiation has also been reported for the P2X2 receptors (Wildman et al., 1998). Two histidine residues, His120 and His213, in the rat P2X2 receptor are involved in the zinc potentiation (Clyne et al., 2002; Nagaya et al., 2005) and are located at the head and dorsal fin domains forming the ATP binding cleft (Figures 2B, S1, and S4D), whereas these histidine residues are not conserved among the P2X4 receptors (Figure S1). The ATP binding causes the cleft closure motion in the ATP binding pocket, which in turn induces the structural change of the body domain for pore opening (Hattori and Gouaux, 2012; Jiang et al., 2012). Accordingly, Zn^{2+} binding to these histidine residues bridges the inter-subunit cleft within the ATP binding pocket to facilitate channel activation (Jiang et al., 2012). In contrast, the M1 site is located far from the ATP binding pocket (Figures 4A, 4C, and 4D), and Zn^{2+} binding to the M1 site would be directly coupled to the structural change of the body domain for pore opening (Figure 6). Therefore, the molecular mechanism of Zn^{2+} potentiation in P2X2 receptors is distinct from that in P2X4 receptors.

Taken together, our results show that allosteric Zn^{2+} binding to the M1 site facilitates the ATP-dependent structural change of the body domain in the extracellular region for pore opening.

Putative Mg^{2+} Modulation Mechanism

We then investigated the possible function of the M2 site in the modulations of P2X receptors by other divalent cations. While ATP exists predominantly as the $MgATP^{2-}$ complex in vivo, a recent electrophysiological analysis demonstrated that distinct subtypes of P2X receptors exhibit differential sensitivities to $MgATP^{2-}$, leading to modulation by Mg^{2+} (Li et al., 2013). The fast-desensitizing P2X receptors, such as P2X1 and P2X3, can be activated by both $MgATP^{2-}$ and Mg^{2+}-free ATP with similar efficacies (Li et al., 2013). In contrast, the slowly desensitizing P2X receptors, such as P2X2, P2X4, and P2X7, can be activated

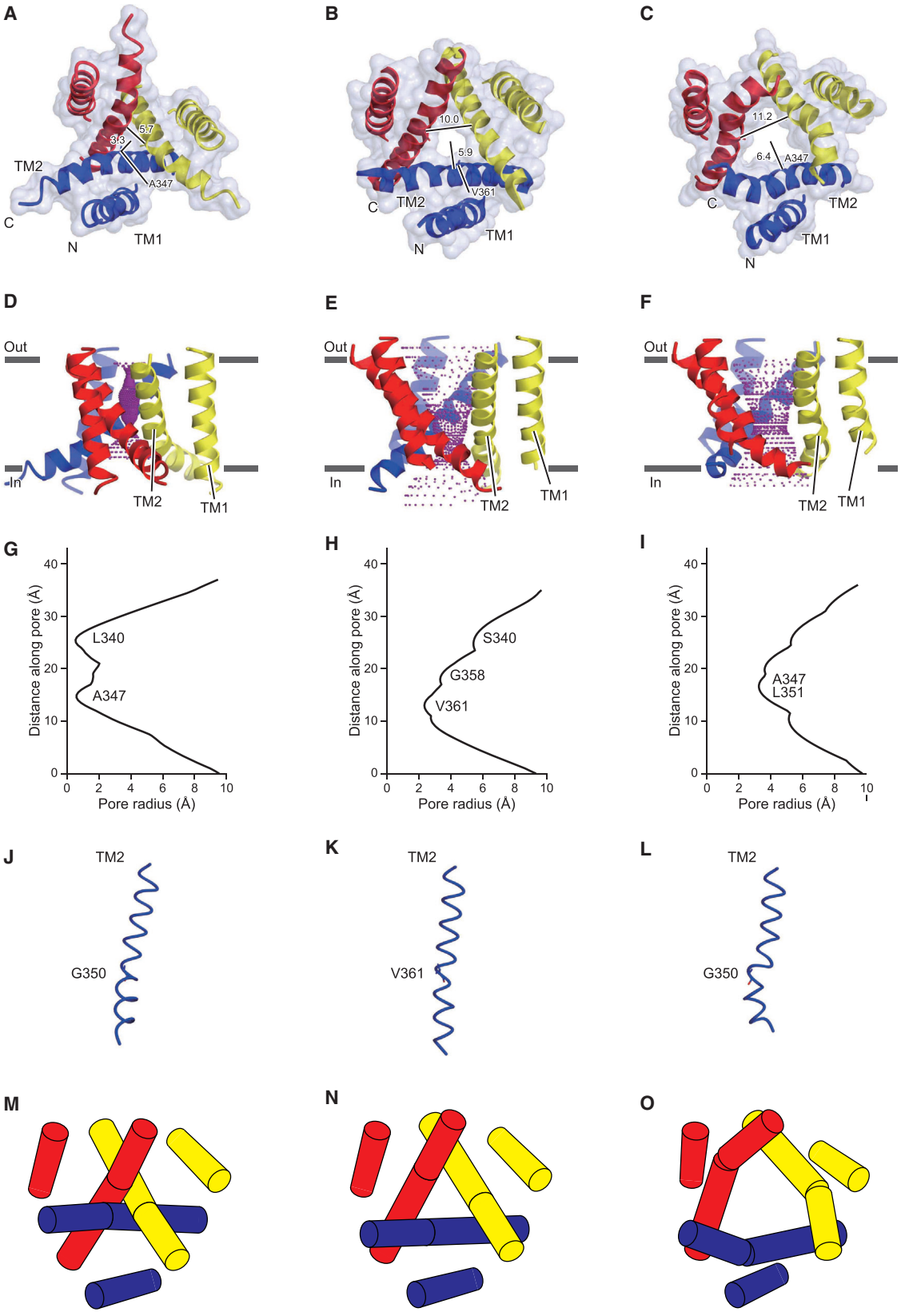

(legend on next page)

by Mg^{2+}-free ATP, but $MgATP^{2-}$ exhibits only low efficacy with these receptors (Li et al., 2013).

The M2 site in the AmP2X structure is coupled with the ATP binding site and bridges the receptor and the phosphate groups of ATP (Figure 4B). The coordination of the divalent cation to the β- and γ-phosphate groups of the ATP in the M2 site is reminiscent of the $MgATP^{2-}$ complex. Furthermore, Asp188 in the M2 site is strictly conserved among the fast-desensitizing P2X1 and P2X3 receptors that exhibit similar sensitivities to both $MgATP^{2-}$ and Mg^{2+}-free ATP (Figure S1). Accordingly, we hypothesized that the M2 site contributes to the accommodation of the $MgATP^{2-}$ complex at the ATP binding site for the $MgATP^{2-}$ sensitivity of these receptors.

To test our hypothesis on the functional role of the M2 site, we performed an electrophysiological analysis with the human P2X1 receptor, which exhibits similar sensitivities to both $MgATP^{2-}$ and Mg^{2+}-free ATP (Li et al., 2013). Because we lack the structure of the P2X1 receptor and the Asp188 at the M2 site in AmP2X, corresponding to Asp170 in P2X1, is located on the loop region (Figure S1), we could not exclude the possibilities that the neighboring Asp171 in P2X1 might be involved in Mg^{2+} recognition or complement the mutation of Asp170. Therefore, we introduced the mutations of both Asp170 and neighboring Asp171 to create the mutant of human P2X1 (^{h}D170A/^{h}D171A) (the superscript "h" refers to human P2X1) for the analysis of the M2 site. We analyzed the dose-response relationships to ATP by the ^{h}WT and the ^{h}D170A/^{h}D171A mutant in the presence of high (5 mM) and low (0.5 mM) extracellular Mg^{2+} concentrations (Figures 5C–5G). The ^{h}WT receptor exhibited similar half-maximal effective concentration (EC_{50}) values for ATP at the high and low extracellular Mg^{2+} concentrations, consistent with the previous electrophysiological report (Figures 5C and 5D) (Li et al., 2013). In contrast, the ^{h}D170A/^{h}D171A mutant exhibited a 5-fold reduction in ATP affinity at the high extracellular Mg^{2+} concentration (EC_{50} = 6.55 ± 1.44 μM) compared to that at the low extracellular Mg^{2+} concentration (EC_{50} = 1.34 ± 0.27 μM) (Figures 5E and 5F). The rat P2X2 receptor, which lacks the M2 site (Figure S1), also showed a Mg^{2+}-dependent shift in the ATP concentration-current amplitude relationship (Li et al., 2013). In addition, the estimated log (K_d) value of the P2X2 receptor for Mg^{2+} calculated from the shift was consistent with the known stability constant of Mg^{2+} binding to ATP, indicating the strong preference for Mg^{2+}-free ATP over $MgATP^{2-}$. Overall, our results suggest that the M2 site, which is coupled with the ATP binding site, may contribute to the differential sensitivities to $MgATP^{2-}$ among subtypes of P2X receptors.

DISCUSSION

In this work, we determined the crystal structure of the invertebrate P2X receptor from the Gulf Coast tick, in the presence of ATP and Zn^{2+} ion, and identified two metal binding sites in the extracellular domain of AmP2X to examine the divalent cation modulation of P2X receptors.

The M1 site, located at the trimer interface, is responsible for Zn^{2+} potentiation by allosterically facilitating the structural change of the body domain in the extracellular region for pore opening (Figures 4A–4D and 6). Zn^{2+} is an essential ion that modulates numerous ion channels, such as NMDA receptors, and is implicated in controlling their physiological functions (Morris and Levenson, 2012). The M1 site is highly conserved among the P2X4 receptors, and consistently, the Zn^{2+} modulation of the P2X4 receptors may be involved in long-term potentiation (Lorca et al., 2011), implying the physiological significance of the M1 site among the P2X4 receptors. In the phylogenetic tree, the invertebrate P2X receptors possessing the M1 site are evolutionarily closer to each other than to the invertebrate P2X receptors lacking the M1 site (Figure S2). The invertebrate P2X receptors lacking the M1 site include those from unicellular organisms, such as the marine green alga *Ostreococcus tauri* and the soil amoeba *Dictyostelium discoideum* (Figure S2). Furthermore, as we mentioned earlier, the invertebrate P2X receptor, LsP2X from the great pond snail, with the M1 site (Figure S1) is also reportedly potentiated by Zn^{2+} ion (Bavan et al., 2012). These findings provide possible insights into how P2X receptors evolutionarily acquired the M1 site-mediated Zn^{2+} potentiation.

In contrast, the other divalent cation binding site, the M2 site, is coupled with the ATP binding site and may contribute to $MgATP^{2-}$ sensitivity among some P2X receptors (Figures 5C–5G). Because ATP predominantly exists as $MgATP^{2-}$ in vivo, it is reasonable that Mg^{2+} ion modulates the ATP-dependent receptor activation in a manner that is directly coupled with ATP binding, rather than through allosteric modulation.

Overall, this work provides structural insights into the divalent cation modulations of the P2X receptors, which form the basis for the diverse physiological functions of this ion channel superfamily.

EXPERIMENTAL PROCEDURES

Expression and Purification

Expression screening of P2X orthologs and further construct optimization were performed with GFP-FSEC and FSEC-based thermostability assay

Figure 3. Structural Comparisons of the Transmembrane Domains

(A–C) The transmembrane domains of apo, closed $\Delta P2X_4$-B_2 (A); ATP-bound $AmP2X_{cryst}$ (B); and ATP-bound $\Delta P2X_4$-C (C) viewed from the intracellular side. A surface model with a cartoon representation is shown for each structure. Amino acid residues involved in the pore constriction region are depicted by stick models. In (A) and (C), the distances between the Cα position of Ala347 and the center of the pore are shown by black lines and numbers (angstroms). In (B), the distances between the Cα position of Val361 and the center of the pore are shown by black lines and numbers (angstroms).

(D–F) Close-up views of the pore domain in apo, closed $\Delta P2X_4$-B_2 (D); ATP-bound $AmP2X_{cryst}$ (E); and ATP-bound $\Delta P2X_4$-C (F) viewed parallel to the membrane.

(G–I) Pore radii for apo, closed $\Delta P2X_4$-B_2 (G); ATP-bound $AmP2X_{cryst}$ (H); and ATP-bound $\Delta P2X_4$-C (I) along the pore center axis.

(J–L) Close-up views of the TM2 helices in apo, closed $\Delta P2X_4$-B_2 (J); ATP-bound $AmP2X_{cryst}$ (K); and ATP-bound $\Delta P2X_4$-C (L). Amino acid residues involved in the pore constriction region are depicted by stick models.

(M–O) Cartoon models of the transmembrane regions in apo, closed $\Delta P2X_4$-B_2 (M); ATP-bound $AmP2X_{cryst}$ (N); and ATP-bound $\Delta P2X_4$-C (O).

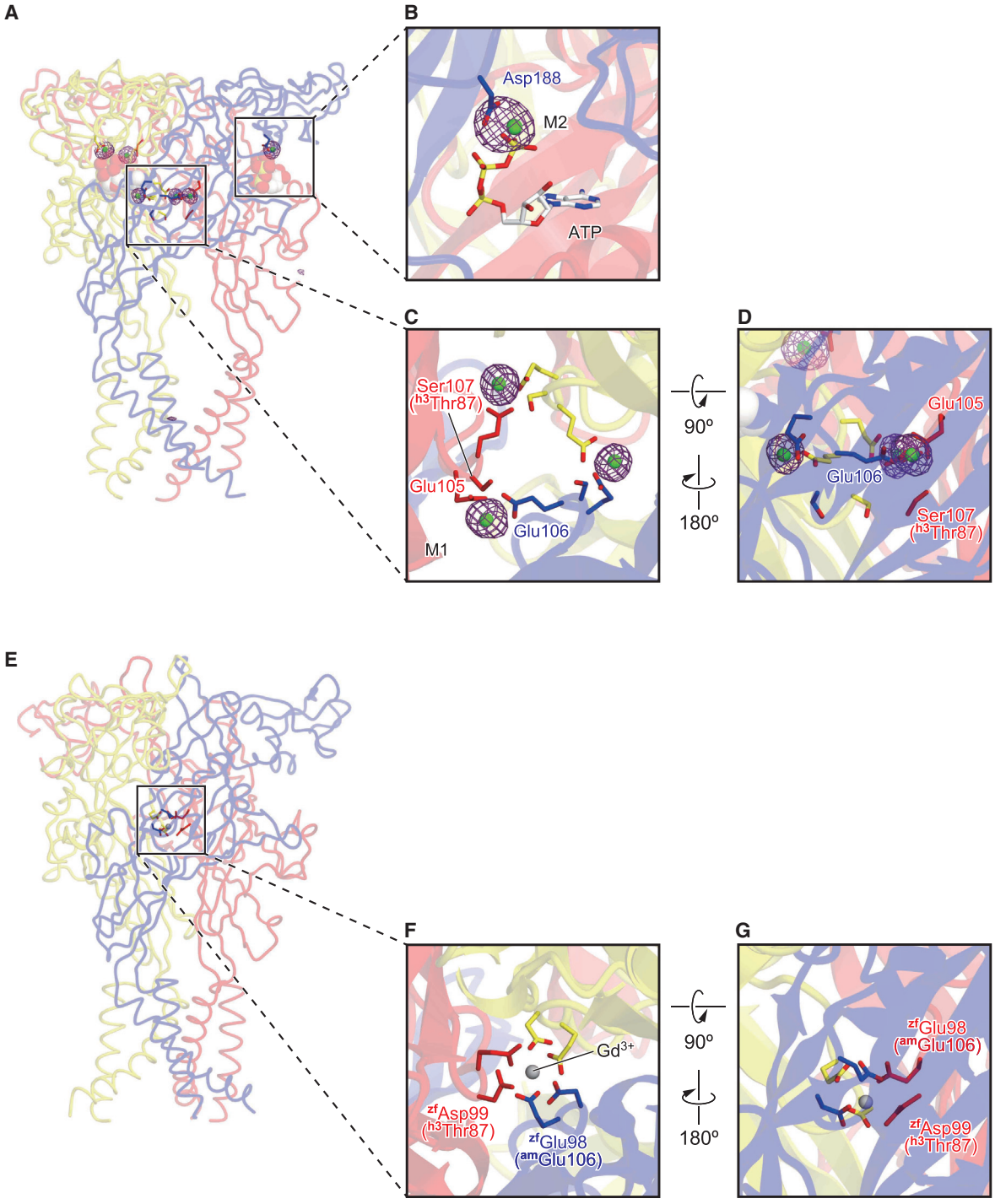

Figure 4. Metal Binding Sites of AmP2X and of apo, Closed zfP2X4

(A) Overall view of the zinc binding sites in the AmP2X structure. The omit $F_o - F_c$ map contoured at 6σ, showing the electron densities of the zinc ions.

(B–D) Close-up views of the zinc binding sites. The anomalous difference Fourier maps contoured at 4σ, showing the electron densities of the zinc ions.

(E) Overall view of the gadolinium binding site in the apo, closed zfP2X4 structure (PDB: 3H9V).

(F and G) Close-up view of the gadolinium binding site. The superscripts "zf," "am," and "h3" refer to zfP2X4, AmP2X, and human P2X3, respectively. The amino acid residues ^{zf}Glu98 and ^{zf}Asp99 correspond to ^{am}Glu106 and ^{am}Ser107 (^{h3}Thr87), respectively.

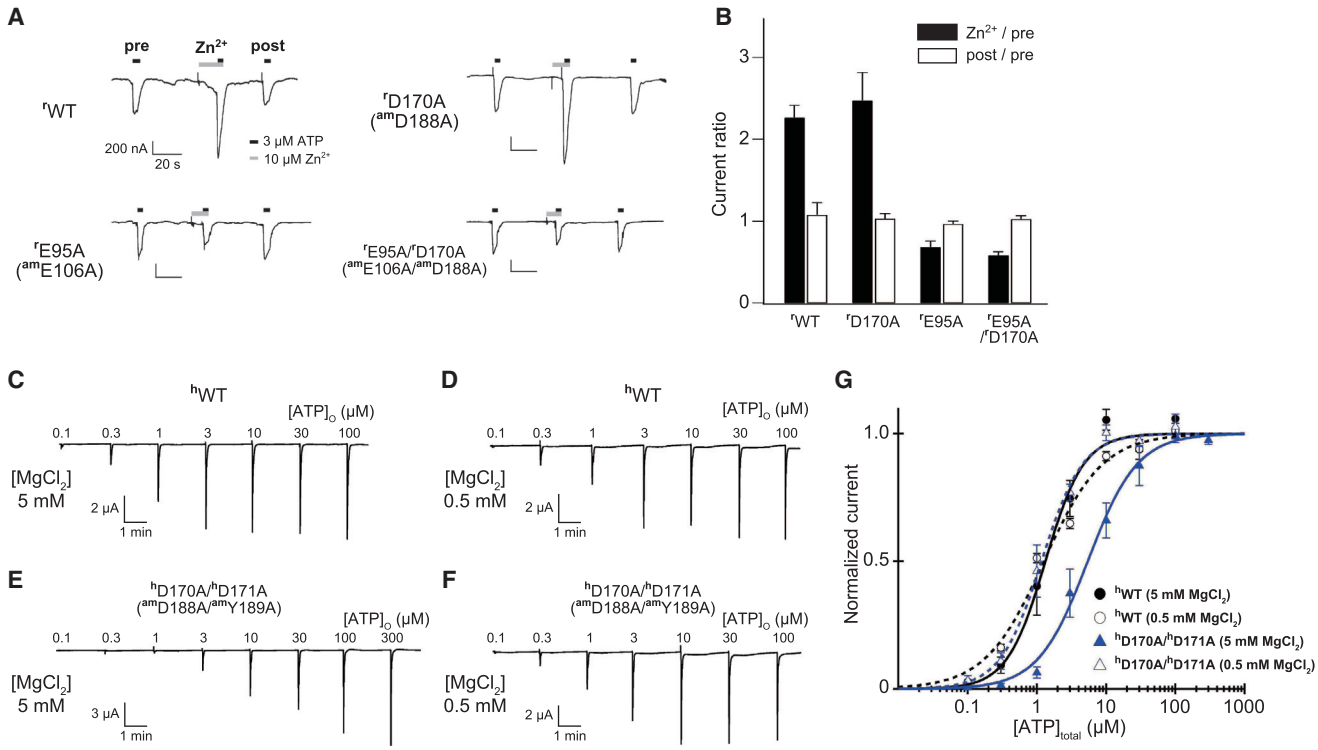

Figure 5. Zn^{2+} and Mg^{2+} Effects on the M1 and M2 Sites

(A) Representative currents of rat P2X4 (rWT) and the zinc binding site mutants evoked by 3 μM ATP in the presence and absence of 10 μM Zn^{2+}.

(B) Accumulated data for the relative current amplitudes in the presence and absence of Zn^{2+}. Bars depict mean + SEM (n = 5–7). The superscripts "r" and "am" refer to the rat P2X4 and AmP2X, respectively. The amino acid residues rGlu95 and rAsp170 correspond to amGlu106 and amAsp188, respectively.

(C–F) Effects of $MgCl_2$ on the ATP-activated currents in human P2X1 WT (hWT) and the hD170A/hD171A (amD188A/amY189A) mutant. (C and D) Representative currents of hWT under the 5 mM $MgCl_2$ conditions (C) and under the 0.5 mM $MgCl_2$ conditions (D). (E and F) Representative currents of hD170A/hD171A (amD188A/amY189A) mutant under the 5 mM $MgCl_2$ conditions (E) and under the 0.5 mM $MgCl_2$ conditions (F). The numbers above the currents indicate the ATP concentrations.

(G) Concentration-response relationships of ATP-evoked currents of hWT under the 5 mM $MgCl_2$ conditions (EC_{50} = 1.65 ± 0.40 μM, n = 6) and under the 0.5 mM $MgCl_2$ conditions (EC_{50} = 1.14 ± 0.09 μM, n = 6) and of the hD170A/hD171A (amD188A/amY189A) mutant under the 5 mM $MgCl_2$ conditions (EC_{50} = 6.55 ± 1.44 μM, n = 7) and under the 0.5 mM $MgCl_2$ conditions (EC_{50} = 1.34 ± 0.27 μM, n = 6). Error bars depict mean ± SEM. The superscripts "h" and "am" refer to the human P2X1 and AmP2X, respectively. The amino acid residues hAsp170 and hAsp171 correspond to amAsp188 and amTyr189, respectively.

(Hattori et al., 2012; Kawate and Gouaux, 2006). We found that the construct ($AmP2X_{cryst}$) from AmP2X (Gene ID: 346469461) was biochemically robust and suitable for crystallization.

The $AmP2X_{cryst}$ construct was subcloned into the pEG BacMam vector, as an N-terminal EGFP fusion with an octa-histidine affinity tag (EGFP-8 × His), and was expressed in HEK293S GnTI$^-$ (N-acetylglucosaminyl-transferase I-negative) cells (Goehring et al., 2014). Cell collection, disruption, and membrane isolation were performed as described previously (Hattori and Gouaux, 2012), except for the use of Tris-buffered saline (TBS) (50 mM Tris [pH 8.0], 150 mM NaCl) supplemented with 5% glycerol. For the purification of $AmP2X_{cryst}$, all buffers were supplemented with 5% glycerol. The membrane fraction was solubilized for 1 hr in TBS, containing 40 mM n-dodecyl-β-D-maltopyranoside (DDM) (Calbiochem). The detergent-soluble fraction was incubated with Talon metal affinity resin (Clontech) and eluted with 250 mM imidazole. After TEV protease digestion and Endo H treatment, to remove the EGFP-8 × His tag and part of the N glycans, the protein was isolated by size-exclusion chromatography on a Superdex 200 10/300 GL column (GE Healthcare) in size-exclusion chromatography buffer (20 mM HEPES [pH 7.0], 100 mM NaCl) containing 5 mM n-decyl-β-D-maltopyranoside (DM) (Anatrace). The peak fractions of the protein were collected and concentrated to 2 mg/ml using a centrifugal filter device (Millipore, 50 kDa molecular weight cutoff).

Crystallization and Data Collection

Before crystallization, 1 mM ATP was added to the protein solutions. The crystals were grown at 4°C with mixtures of 1:1 or 2:1 (v/v) ratios of protein and reservoir solutions by the vapor diffusion method. The crystals of $AmP2X_{cryst}$ appeared in 8%–11% (w/v) PEG 8000, 0.05 M zinc acetate, and 0.05 M MES (pH 6.0). The crystals were flash-frozen in liquid nitrogen for X-ray diffraction experiments. The X-ray diffraction data were collected at 100 K at BL41XU of SPring-8 and were processed using HKL2000 (Otwinowski and Minor, 1997).

Structure Determination

The structure of $AmP2X_{cryst}$ was obtained by molecular replacement with Phaser (McCoy et al., 2007) using the ATP-bound $\Delta P2X_4$-C structure (PDB: 4DW1) as the template. The determined structure was further refined by using the programs PHENIX (Afonine et al., 2012) and COOT (Emsley et al., 2010). Crystallographic data and refinement statistics are presented in Table S1. All figures were prepared with CueMol software (http://www.cuemol.org). In Figure 3, the pore plots were generated using HOLE software (Smart et al., 1996).

TEVC Recording

The *Xenopus* oocytes were incubated at 18°C in Barth's solution, containing 88 mM NaCl, 1 mM KCl, 2.4 mM $NaHCO_3$, 10 mM HEPES, 0.33 mM

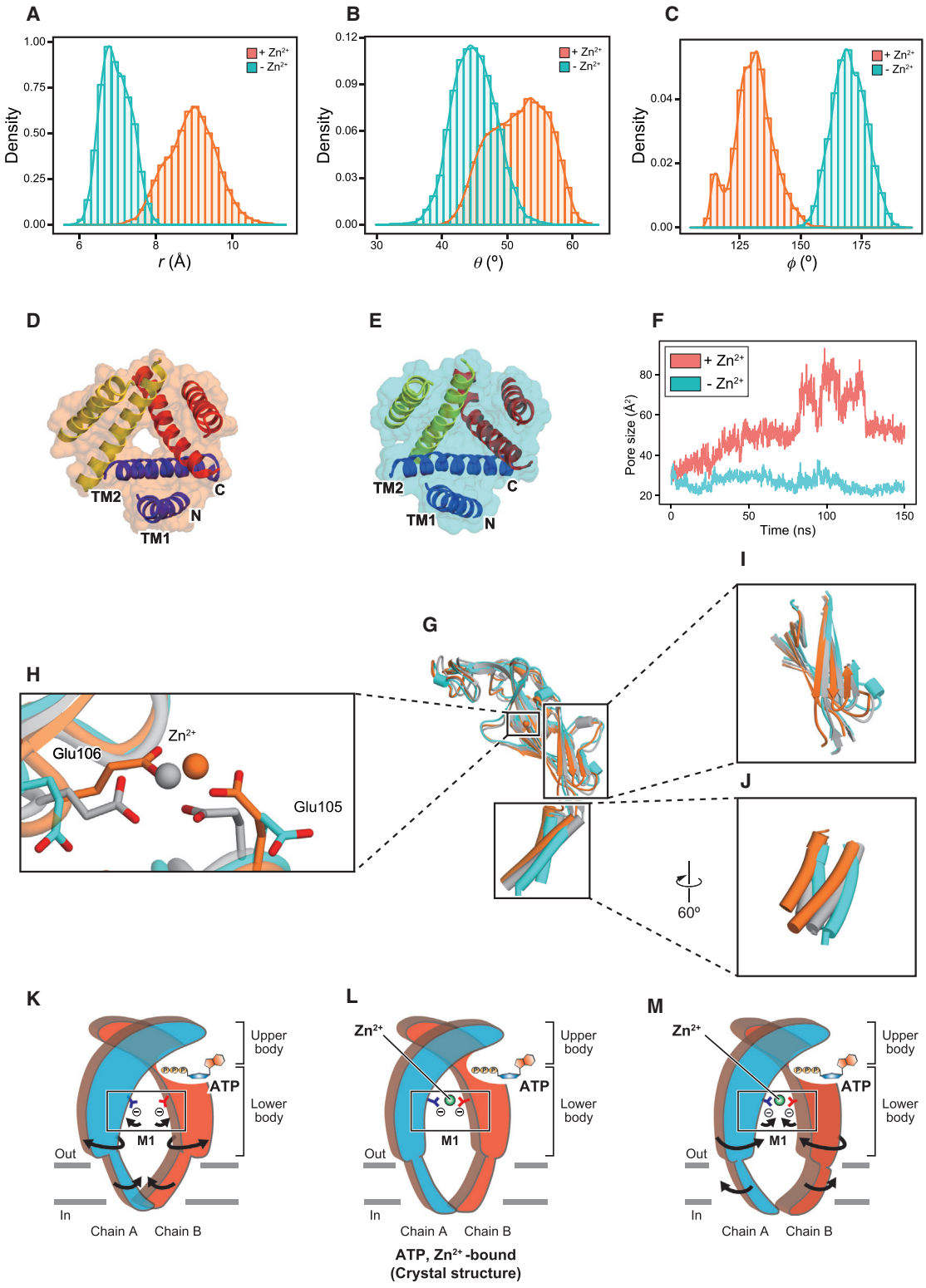

Figure 6. Zinc Modulation Mechanism

(A–C) Distributions of *r* (A), θ (B), and ϕ (C) are displayed. Orange distributions indicate the results of the MD simulations in the presence of Zn^{2+} at the M1 site, and cyan distributions indicate the results of the MD simulations in the absence of Zn^{2+} at the M1 site.

(legend continued on next page)

$Ca(NO_3)_2$, 0.41 mM $CaCl_2$, and 0.82 mM $MgSO_4$ (pH 7.4); supplemented with 50 μg/ml gentamicin; and were used for recording after 4–7 days. The standard bath solution for recordings contained 100 mM NaCl, 5 mM HEPES, 2 mM $MgCl_2$ (pH 7.3), and ATP and was freshly prepared each day. In Figures 5C–5G, the sensitivity to $MgATP^{2-}$ was analyzed with two recording solutions, containing 100 mM NaCl, 5 mM HEPES (pH 7.3), and either 5 mM or 0.5 mM $MgCl_2$. Under these conditions, [$MgATP^{2-}$] and [Mg^{2+}-free ATP] increase linearly with increasing [ATP] applied. [Mg^{2+}-free ATP] in the high (5 mM) Mg^{2+} solution is about eight or nine times lower than that in the low (0.5 mM) Mg^{2+} solution, while [$MgATP^{2-}$] is exactly the same between the two solutions. Hence, the difference in the ATP dose response is considered to be derived from the reduction of the $MgATP^{2-}$ binding to the mutant channel (Figure 5G). A small amount of divalent cation was needed to suppress the endogenous currents of the oocytes, and 0.5 mM $MgCl_2$ was sufficient in this experiment. Oocytes were held at −70 mV with a bath-clamp amplifier (OC-725C, Warner) with the direct current gain booster turned on, and the macroscopic currents were recorded and analyzed using pClamp 10 software (Molecular Devices), as described previously (Fujiwara et al., 2009). Actual clamped membrane potentials were also monitored during the recordings, and data with an error of more than 1 mV from the command potentials were discarded. When the data were contaminated by endogenous currents and/or leak currents, they were also discarded. In Figures 5A and 5B, the ratios of the current amplitudes in the presence or absence of $ZnCl_2$ to the amplitude before Zn^{2+} application were analyzed. In Figures S5A–S5D, a dataset from an identical oocyte was used for the analysis of the half-maximal inhibitory concentration value for $GdCl_3$.

Confocal Microscopy

The hemagglutinin-tagged, EGFP-fused AmP2X WT and mutants were injected in oocytes. At 3–4 days after injection, the oocytes were imaged using an FV300 confocal microscope (Olympus) equipped with a ×20/0.5 numerical aperture objective under TEVC. The bath solution was the same as that used for the TEVC recordings (see TEVC Recording). Images were collected every 30 s for 25 min using the Fluoview software (Olympus). Fluorescence intensity was calculated for each image and plotted against time, and the data were reported as mean ± SEM (Figure S3).

Radiolabeled ATP Binding Experiments

The EGFP-fusion $AmP2X_{cryst}$ construct was expressed and purified as described previously; concentrated; dialyzed overnight at 4°C to remove impurities in dialysis buffer containing 20 mM HEPES (pH 7.0), 100 mM NaCl, 5% glycerol, and 1 mM DDM; and stored at −80°C before use. ATP binding experiments were performed in the same manner as described previously (Hattori and Gouaux, 2012), except for the use of dialysis buffer containing 20 mM HEPES (pH 7.0), 80 mM NaCl, 20 mM KCl, 1 mM DDM, and 1,000–3,000 nM ^{3}H-ATP (PerkinElmer), in which the radiolabeled ATP was diluted with unlabeled ATP at a ratio of 1:4. The entire experiment was performed in triplicate. Data were fit to a sigmoidal dose-response equation.

MD Simulations

The simulation system included the $AmP2X_{cryst}$ trimer, 1-palmitoyl-2-oleoyl-phosphatidylcholine (POPC), ATP, Zn^{2+} ions, water molecules, and 150 mM NaCl. The missing atoms, including hydrogens in the protein, were added with the program VMD (Humphrey et al., 1996). The periodic boundary system, including the explicit solvent and the POPC lipid bilayer, was prepared. The size of the simulation box was 128 × 128 × 148 Å. The net charge of the system was neutralized by adding chloride and sodium ions. The topologies and force field parameters from CHARMM36 were used (Klauda et al., 2010). MD simulations were performed with the program NAMD 2.9 (Phillips et al., 2005). The system was first energy minimized for 1,000 steps with fixed positions for the non-hydrogen atoms and then for another 1,000 steps with 10 kcal/mol restraints for the non-hydrogen atoms. Next, we performed an equilibration run for 0.5 ns in the NVT ensemble (310 K, 128 × 128 × 148 Å volume) with 10 kcal/mol restraints for protein non-hydrogen atoms, ATP, and Zn^{2+}, followed by an equilibration run for 1.0 ns in the NPT ensemble (310 K, 1 atm), with the same restraints. Finally, we performed equilibration runs for 1.0 ns in the NPT ensemble, with the bond length restraints between Zn^{2+} ions or ATP and the protein side chain: (1) ATP N1 and Thr206 OG1, (2) M2 and ATP OG1, (3) M1 and Glu105, (4) M1 and Glu106, and (5) M2 and Asp188 of the adjacent chain. These restrained bond lengths are based on those observed in the crystal structure of $AmP2X_{cryst}$. The production process was performed for 150 ns, with the same bond length restraints. Constant temperature was maintained by using Langevin dynamics. Constant pressure was maintained by using the Langevin piston Nosé-Hoover method (Feller et al., 1995). Long-range electrostatic interactions were calculated using the particle mesh Ewald method (Darden et al., 1993).

ACCESSION NUMBERS

The accession number for the ATP-bound $AmP2X_{cryst}$ structure reported in this paper is PDB: 5F1C.

SUPPLEMENTAL INFORMATION

Supplemental Information includes five figures and one table and can be found with this article online at http://dx.doi.org/10.1016/j.celrep.2015.12.087.

AUTHOR CONTRIBUTIONS

G.K., Y.F., and M.H. performed experiments. M.T. and R.I. performed the MD simulation. N.D. and Y.N.-N. assisted with the structure determination. G.K., M.H., and O.N. wrote the manuscript. M.H. and O.N. supervised all research.

ACKNOWLEDGMENTS

We thank T. Nishizawa and H.E. Kato for critical comments on the manuscript, A. Kurabayashi for technical support, and the beamline staff members at BL41XU of SPring-8 (Hyogo, Japan) for technical assistance during data collection. The pEG BacMam vector was kindly provided by Dr. Eric Gouaux (Oregon Health and Science University). The computations were performed with the mini-K super computer system at the SACLA facility and the NIG supercomputer at ROIS National Institute of Genetics. This work was supported by the Platform for Drug Discovery, Informatics, and Structural Life Science from the Ministry of Education, Culture, Sports, Science and Technology (MEXT); by JSPS KAKENHI (Grant Nos. 22117007, 24227004, and 25291011); and by grants from PRESTO, JST, to M.H. and the FIRST program and CREST, JST, to O.N.

(D and E) The transmembrane domain of ATP-bound $AmP2X_{cryst}$ after the 150 ns MD simulations in the presence of Zn^{2+} at the M1 site (D) and in the absence of Zn^{2+} at the M1 site (E). Each structure is viewed from the extracellular side. A surface model containing the cartoon representation is shown for each structure.
(F) The time course of the pore sizes of ATP-bound $AmP2X_{cryst}$ through the 150 ns MD simulations. The orange graph shows the results of the simulations in the presence of Zn^{2+} at the M1 site, and the cyan graph shows the results of the simulations in the absence of Zn^{2+} at the M1 site. The pore sizes are defined by the triangular dimensions formed by the three Cα positions of Val362 from each subunit.
(G–J) Subunit comparisons of ATP-bound $AmP2X_{cryst}$ before the MD simulation (gray) and after the 150 ns MD simulations in the presence of Zn^{2+} at the M1 sites (orange) and in the absence of Zn^{2+} at the M1 sites (cyan). Close-up views of the M1 site (H), the lower body (I), and the fluke (J) are shown in each box.
(K–M) Cartoon models of the Zn^{2+}-dependent stabilization mechanism of the ATP-bound $AmP2X_{cryst}$ open state. (K) The model after the 150 ns MD simulation in the absence of Zn^{2+} at the M1 site. (L) The crystal structure model of ATP, Zn^{2+}-bound $AmP2X_{cryst}$. (M) The model after the 150 ns MD simulation in the presence of Zn^{2+} at the M1 site. In cartoon models (K) and (M), the black arrows denote the movement from the crystal structure model (L).

Received: August 4, 2015
Revised: November 3, 2015
Accepted: December 18, 2015
Published: January 21, 2016

REFERENCES

Afonine, P.V., Grosse-Kunstleve, R.W., Echols, N., Headd, J.J., Moriarty, N.W., Mustyakimov, M., Terwilliger, T.C., Urzhumtsev, A., Zwart, P.H., and Adams, P.D. (2012). Towards automated crystallographic structure refinement with phenix.refine. Acta Crystallogr. D Biol. Crystallogr. *68*, 352–367.

Agboh, K.C., Webb, T.E., Evans, R.J., and Ennion, S.J. (2004). Functional characterization of a P2X receptor from *Schistosoma mansoni*. J. Biol. Chem. *279*, 41650–41657.

Bavan, S., Straub, V.A., Blaxter, M.L., and Ennion, S.J. (2009). A P2X receptor from the tardigrade species *Hypsibius dujardini* with fast kinetics and sensitivity to zinc and copper. BMC Evol. Biol. *9*, 17.

Bavan, S., Straub, V.A., Webb, T.E., and Ennion, S.J. (2012). Cloning and characterization of a P2X receptor expressed in the central nervous system of *Lymnaea stagnalis*. PLoS ONE *7*, e50487.

Bernier, L.P., Ase, A.R., Chevallier, S., Blais, D., Zhao, Q., Boué-Grabot, E., Logothetis, D., and Séguéla, P. (2008). Phosphoinositides regulate P2X4 ATP-gated channels through direct interactions. J. Neurosci. *28*, 12938–12945.

Bo, X., Schoepfer, R., and Burnstock, G. (2000). Molecular cloning and characterization of a novel ATP P2X receptor subtype from embryonic chick skeletal muscle. J. Biol. Chem. *275*, 14401–14407.

Brake, A.J., Wagenbach, M.J., and Julius, D. (1994). New structural motif for ligand-gated ion channels defined by an ionotropic ATP receptor. Nature *371*, 519–523.

Burnstock, G. (2006). Pathophysiology and therapeutic potential of purinergic signaling. Pharmacol. Rev. *58*, 58–86.

Burnstock, G., and Ralevic, V. (2014). Purinergic signaling and blood vessels in health and disease. Pharmacol. Rev. *66*, 102–192.

Chen, C.C., Akopian, A.N., Sivilotti, L., Colquhoun, D., Burnstock, G., and Wood, J.N. (1995). A P2X purinoceptor expressed by a subset of sensory neurons. Nature *377*, 428–431.

Clyne, J.D., LaPointe, L.D., and Hume, R.I. (2002). The role of histidine residues in modulation of the rat P2X(2) purinoceptor by zinc and pH. J. Physiol. *539*, 347–359.

Dai, J., and Zhou, H.X. (2014). General rules for the arrangements and gating motions of pore-lining helices in homomeric ion channels. Nat. Commun. *5*, 4641.

Darden, T., York, D., and Pedersen, L. (1993). Particle mesh Ewald: an N·log(N) method for Ewald sums in large systems. J. Chem. Phys. *98*, 10089.

Egan, T.M., Samways, D.S., and Li, Z. (2006). Biophysics of P2X receptors. Pflugers Arch. *452*, 501–512.

Emsley, P., Lohkamp, B., Scott, W.G., and Cowtan, K. (2010). Features and development of Coot. Acta Crystallogr. D Biol. Crystallogr. *66*, 486–501.

Ennion, S., Hagan, S., and Evans, R.J. (2000). The role of positively charged amino acids in ATP recognition by human P2X(1) receptors. J. Biol. Chem. *275*, 29361–29367.

Feller, S.E., Zhang, Y., Pastor, R.W., and Brooks, B.R. (1995). Constant pressure molecular dynamics simulation: the Langevin piston method. J. Chem. Phys. *103*, 4613.

Fountain, S.J., Parkinson, K., Young, M.T., Cao, L., Thompson, C.R., and North, R.A. (2007). An intracellular P2X receptor required for osmoregulation in *Dictyostelium discoideum*. Nature *448*, 200–203.

Fujiwara, Y., and Kubo, Y. (2006). Regulation of the desensitization and ion selectivity of ATP-gated P2X2 channels by phosphoinositides. J. Physiol. *576*, 135–149.

Fujiwara, Y., Keceli, B., Nakajo, K., and Kubo, Y. (2009). Voltage- and [ATP]-dependent gating of the P2X(2) ATP receptor channel. J. Gen. Physiol. *133*, 93–109.

Garcia-Guzman, M., Soto, F., Gomez-Hernandez, J.M., Lund, P.E., and Stühmer, W. (1997). Characterization of recombinant human P2X4 receptor reveals pharmacological differences to the rat homologue. Mol. Pharmacol. *51*, 109–118.

Gever, J.R., Cockayne, D.A., Dillon, M.P., Burnstock, G., and Ford, A.P. (2006). Pharmacology of P2X channels. Pflugers Arch. *452*, 513–537.

Goehring, A., Lee, C.H., Wang, K.H., Michel, J.C., Claxton, D.P., Baconguis, I., Althoff, T., Fischer, S., Garcia, K.C., and Gouaux, E. (2014). Screening and large-scale expression of membrane proteins in mammalian cells for structural studies. Nat. Protoc. *9*, 2574–2585.

Hattori, M., and Gouaux, E. (2012). Molecular mechanism of ATP binding and ion channel activation in P2X receptors. Nature *485*, 207–212.

Hattori, M., Hibbs, R.E., and Gouaux, E. (2012). A fluorescence-detection size-exclusion chromatography-based thermostability assay for membrane protein precrystallization screening. Structure *20*, 1293–1299.

Heymann, G., Dai, J., Li, M., Silberberg, S.D., Zhou, H.X., and Swartz, K.J. (2013). Inter- and intrasubunit interactions between transmembrane helices in the open state of P2X receptor channels. Proc. Natl. Acad. Sci. USA *110*, E4045–E4054.

Humphrey, W., Dalke, A., and Schulten, K. (1996). VMD: visual molecular dynamics. J Mol Graph *14*, 33–38.

Jarvis, M.F., and Khakh, B.S. (2009). ATP-gated P2X cation-channels. Neuropharmacology *56*, 208–215.

Jensik, P., and Cox, T. (2002). ATP-induced internalization of amphibian epithelial P2X receptors is linked to channel opening. Pflugers Arch. *444*, 795–800.

Jiang, L.H., Rassendren, F., Surprenant, A., and North, R.A. (2000). Identification of amino acid residues contributing to the ATP-binding site of a purinergic P2X receptor. J. Biol. Chem. *275*, 34190–34196.

Jiang, R., Taly, A., Lemoine, D., Martz, A., Cunrath, O., and Grutter, T. (2012). Tightening of the ATP-binding sites induces the opening of P2X receptor channels. EMBO J. *31*, 2134–2143.

Jiang, R., Taly, A., and Grutter, T. (2013). Moving through the gate in ATP-activated P2X receptors. Trends Biochem. Sci. *38*, 20–29.

Kawate, T., and Gouaux, E. (2006). Fluorescence-detection size-exclusion chromatography for precrystallization screening of integral membrane proteins. Structure *14*, 673–681.

Kawate, T., Michel, J.C., Birdsong, W.T., and Gouaux, E. (2009). Crystal structure of the ATP-gated P2X(4) ion channel in the closed state. Nature *460*, 592–598.

Khakh, B.S., and North, R.A. (2012). Neuromodulation by extracellular ATP and P2X receptors in the CNS. Neuron *76*, 51–69.

Klauda, J.B., Venable, R.M., Freites, J.A., O'Connor, J.W., Tobias, D.J., Mondragon-Ramirez, C., Vorobyov, I., MacKerell, A.D., Jr., and Pastor, R.W. (2010). Update of the CHARMM all-atom additive force field for lipids: validation on six lipid types. J. Phys. Chem. B *114*, 7830–7843.

Lewis, C.J., and Evans, R.J. (2000). Lack of run-down of smooth muscle P2X receptor currents recorded with the amphotericin permeabilized patch technique, physiological and pharmacological characterization of the properties of mesenteric artery P2X receptor ion channels. Br. J. Pharmacol. *131*, 1659–1666.

Li, M., Silberberg, S.D., and Swartz, K.J. (2013). Subtype-specific control of P2X receptor channel signaling by ATP and Mg2+. Proc. Natl. Acad. Sci. USA *110*, E3455–E3463.

Lorca, R.A., Rozas, C., Loyola, S., Moreira-Ramos, S., Zeise, M.L., Kirkwood, A., Huidobro-Toro, J.P., and Morales, B. (2011). Zinc enhances long-term potentiation through P2X receptor modulation in the hippocampal CA1 region. Eur. J. Neurosci. *33*, 1175–1185.

Lörinczi, É., Bhargava, Y., Marino, S.F., Taly, A., Kaczmarek-Hájek, K., Barrantes-Freer, A., Dutertre, S., Grutter, T., Rettinger, J., and Nicke, A. (2012). Involvement of the cysteine-rich head domain in activation and desensitization of the P2X1 receptor. Proc. Natl. Acad. Sci. USA *109*, 11396–11401.

Marquez-Klaka, B., Rettinger, J., Bhargava, Y., Eisele, T., and Nicke, A. (2007). Identification of an intersubunit cross-link between substituted cysteine residues located in the putative ATP binding site of the P2X1 receptor. J. Neurosci. *27*, 1456–1466.

McCoy, A.J., Grosse-Kunstleve, R.W., Adams, P.D., Winn, M.D., Storoni, L.C., and Read, R.J. (2007). Phaser crystallographic software. J. Appl. Cryst. *40*, 658–674.

Miller, P.S., and Smart, T.G. (2010). Binding, activation and modulation of Cys-loop receptors. Trends Pharmacol. Sci. *31*, 161–174.

Mo, G., Bernier, L.P., Zhao, Q., Chabot-Doré, A.J., Ase, A.R., Logothetis, D., Cao, C.Q., and Séguéla, P. (2009). Subtype-specific regulation of P2X3 and P2X2/3 receptors by phosphoinositides in peripheral nociceptors. Mol. Pain *5*, 47.

Morris, D.R., and Levenson, C.W. (2012). Ion channels and zinc: mechanisms of neurotoxicity and neurodegeneration. J. Toxicol. *2012*, 785647.

Nagaya, N., Tittle, R.K., Saar, N., Dellal, S.S., and Hume, R.I. (2005). An intersubunit zinc binding site in rat P2X2 receptors. J. Biol. Chem. *280*, 25982–25993.

Nakazawa, K., and Ohno, Y. (1997). Effects of neuroamines and divalent cations on cloned and mutated ATP-gated channels. Eur. J. Pharmacol. *325*, 101–108.

North, R.A. (2002). Molecular physiology of P2X receptors. Physiol. Rev. *82*, 1013–1067.

North, R.A., and Jarvis, M.F. (2013). P2X receptors as drug targets. Mol. Pharmacol. *83*, 759–769.

Otwinowski, Z., and Minor, W. (1997). Processing of X-ray diffraction data collected in oscillation mode. Macromol. Crystallogr. A *276*, 307–326.

Phillips, J.C., Braun, R., Wang, W., Gumbart, J., Tajkhorshid, E., Villa, E., Chipot, C., Skeel, R.D., Kalé, L., and Schulten, K. (2005). Scalable molecular dynamics with NAMD. J. Comput. Chem. *26*, 1781–1802.

Raouf, R., Blais, D., and Séguéla, P. (2005). High zinc sensitivity and pore formation in an invertebrate P2X receptor. Biochim. Biophys. Acta *1669*, 135–141.

Richards-Williams, C., Contreras, J.L., Berecek, K.H., and Schwiebert, E.M. (2008). Extracellular ATP and zinc are co-secreted with insulin and activate multiple P2X purinergic receptor channels expressed by islet beta-cells to potentiate insulin secretion. Purinergic Signal. *4*, 393–405.

Roberts, J.A., and Evans, R.J. (2004). ATP binding at human P2X1 receptors. Contribution of aromatic and basic amino acids revealed using mutagenesis and partial agonists. J. Biol. Chem. *279*, 9043–9055.

Roberts, J.A., and Evans, R.J. (2006). Contribution of conserved polar glutamine, asparagine and threonine residues and glycosylation to agonist action at human P2X1 receptors for ATP. J. Neurochem. *96*, 843–852.

Roberts, J.A., and Evans, R.J. (2007). Cysteine substitution mutants give structural insight and identify ATP binding and activation sites at P2X receptors. J. Neurosci. *27*, 4072–4082.

Roberts, J.A., Digby, H.R., Kara, M., El Ajouz, S., Sutcliffe, M.J., and Evans, R.J. (2008). Cysteine substitution mutagenesis and the effects of methanethiosulfonate reagents at P2X2 and P2X4 receptors support a core common mode of ATP action at P2X receptors. J. Biol. Chem. *283*, 20126–20136.

Roberts, J.A., Allsopp, R.C., El Ajouz, S., Vial, C., Schmid, R., Young, M.T., and Evans, R.J. (2012). Agonist binding evokes extensive conformational changes in the extracellular domain of the ATP-gated human P2X1 receptor ion channel. Proc. Natl. Acad. Sci. USA *109*, 4663–4667.

Samways, D.S., Li, Z., and Egan, T.M. (2014). Principles and properties of ion flow in P2X receptors. Front. Cell. Neurosci. *8*, 6.

Séguéla, P., Haghighi, A., Soghomonian, J.J., and Cooper, E. (1996). A novel neuronal P2x ATP receptor ion channel with widespread distribution in the brain. J. Neurosci. *16*, 448–455.

Smart, O.S., Neduvelil, J.G., Wang, X., Wallace, B.A., and Sansom, M.S. (1996). HOLE: a program for the analysis of the pore dimensions of ion channel structural models. J. Mol. Graph. *14*, 354–360, 376.

Soto, F., Garcia-Guzman, M., Gomez-Hernandez, J.M., Hollmann, M., Karschin, C., and Stühmer, W. (1996). P2X4: an ATP-activated ionotropic receptor cloned from rat brain. Proc. Natl. Acad. Sci. USA *93*, 3684–3688.

Surprenant, A., and North, R.A. (2009). Signaling at purinergic P2X receptors. Annu. Rev. Physiol. *71*, 333–359.

Traynelis, S.F., Wollmuth, L.P., McBain, C.J., Menniti, F.S., Vance, K.M., Ogden, K.K., Hansen, K.B., Yuan, H., Myers, S.J., and Dingledine, R. (2010). Glutamate receptor ion channels: structure, regulation, and function. Pharmacol. Rev. *62*, 405–496.

Valera, S., Hussy, N., Evans, R.J., Adami, N., North, R.A., Surprenant, A., and Buell, G. (1994). A new class of ligand-gated ion channel defined by P2x receptor for extracellular ATP. Nature *371*, 516–519.

Wildman, S.S., King, B.F., and Burnstock, G. (1998). Zn2+ modulation of ATP-responses at recombinant P2X2 receptors and its dependence on extracellular pH. Br. J. Pharmacol. *123*, 1214–1220.

Zhao, W.S., Wang, J., Ma, X.J., Yang, Y., Liu, Y., Huang, L.D., Fan, Y.Z., Cheng, X.Y., Chen, H.Z., Wang, R., and Yu, Y. (2014). Relative motions between left flipper and dorsal fin domains favour P2X4 receptor activation. Nat. Commun. *5*, 4189.